

# Preparation, Structural Analysis, and Tunability of Optical and Dielectric Characteristics of Mn–modified SrLaLiTeO<sub>6</sub> Double Perovskite

MUHAMMAD ZHARFAN MOHD HALIZAN (✉ [Halizanzharfan@yahoo.com](mailto:Halizanzharfan@yahoo.com))

Universiti Teknologi MARA <https://orcid.org/0000-0003-4436-7800>

ZAKIAH MOHAMED

Universiti Teknologi MARA

AHMAD KAMAL HAYATI YAHYA

Universiti Teknologi MARA

---

## Nano Express

**Keywords:** Double perovskites, structural properties, optical properties, dielectric properties

**Posted Date:** February 4th, 2021

**DOI:** <https://doi.org/10.21203/rs.3.rs-159986/v1>

**License:**  This work is licensed under a Creative Commons Attribution 4.0 International License.

[Read Full License](#)

---

---

# Preparation, structural analysis, and tunability of optical and dielectric characteristics of Mn–modified SrLaLiTeO<sub>6</sub> double perovskite

M. Z. M. Halizan, Z. Mohamed\*, and A. K. Yahya

*Faculty of Applied Sciences, Universiti Teknologi MARA, 40450, Shah Alam, Selangor, Malaysia.*

\* Corresponding author E-mail: [zakiah626@uitm.edu.my](mailto:zakiah626@uitm.edu.my)

**Keywords:** Double perovskites; structural properties; optical properties; dielectric properties

---

## 1 Abstract

2 SrLaLiTe<sub>1-x</sub>Mn<sub>x</sub>O<sub>6</sub> ( $x = 0.02, 0.04, 0.06, 0.08, 0.10$ ) double perovskites have been prepared using solid state method. Studies  
3 on structural by applying X–ray diffraction (XRD) characterization found that all compounds formed in monoclinic,  $P2_1/n$   
4 symmetry with reduction of lattice parameters and unit cell volume as dopant concentration increased. The formation of  
5 Te<sup>6+</sup>/Mn<sup>6+</sup>–O–Li<sup>+</sup> octahedral structure can be confirmed with the presence of peaks at certain wavenumbers indicating  
6 vibrations of Te–O or Mn–O bonds. As dopant concentration increased, field emission scanning electron microscope  
7 (FESEM) characterization found that the increasing trend of formation in grains sizes from  $x = 0.02$  to  $x = 0.08$ , and its  
8 effects towards dielectric properties which were conducted by electrochemical impedance spectroscopy (EIS) studies were  
9 discussed in this paper. Other discussions included were regarding the significant effect of dopant towards optical band  
10 gap,  $E_{opt}$  and absorption frequencies of prepared compounds compared to pristine compound indicating its promising  
11 potential for optoelectronic device application.

12

13

## 1. Introduction

14 Research and studies regarding perovskites have been instigated extensively due to its promising  
15 abilities such as superconducting, conductivity, magnetoresistance and ferroelectric. Pertaining to these  
16 astounding characteristics, they are growing appeals for applications in sensors [1–3], capacitors [4],  
17 microwave resonators [5–7] and solar cells [8–11]. Double perovskites oxides introduced an ordered  
18 rock-salt like arrangement of corner–sharing BO<sub>6</sub> and B'O<sub>6</sub> units in the crystal structure. They are  
19 basically comprised of A<sub>2</sub>BB'O<sub>6</sub> or AA'BB'O<sub>6</sub> configuration where A or A' are alkaline–earth or rare–  
20 earth metals in Group I or Group II while B and B' are transition metals. These configurations were  
21 derived from conventional ABO<sub>3</sub> perovskites where six out of twelve A–site cations and six B–site  
22 cations replaced by appropriate A'– and B'–sites cations, respectively. As double perovskites have more

23 sites for substitutions with additional A'– or B'–sites compared to conventional perovskites, they can  
24 have substantial advantages for instance higher Curie temperature ( $T_C$ ) such as  $\text{Sr}_2\text{CrReO}_6$  and  
25  $\text{Ba}_2\text{FeMoO}_6$  with  $T_C$  above 300 K [12, 13] compared to perovskites like  $\text{RCu}_3\text{Mn}_4\text{O}_{12}$  and  $\text{Sr}_{0.9}\text{Sn}_{0.1}\text{TiO}_3$   
26 that possesses  $T_C$  of 50 K and 200 K, respectively [14, 15]. The field has gradually broadened as  
27 tellurium based double perovskites,  $AA'BTeO_6$  has been studied and reported to have relatively good  
28 dielectric properties [16–19]. Variety of discussions which consisted of densification, grain size or  
29 polarizability aspects of A–site cations has been included in these studies. Double perovskites in  
30  $AA'BB'O_6$  form that have 1:1 B-site ordering has been reported to have potential in dielectric application  
31 [19]. Furthermore, double perovskites in  $AA'BB'O_6$  configuration and form polar  $P2_1$  space group  
32 symmetry can be related to existence of ferroelectric or good dielectric properties [20]. Since  
33  $\text{SrLaLiTeO}_6$  claimed to consist of the perfect 1:1 B site ordering of  $\text{Te}^{6+}/\text{Li}^+$  and monoclinic  $P2_1/n$   
34 structure [21] that is similar to that in the  $\text{SrBiLiTeO}_6$ ,  $\text{BaBiLiTeO}_6$ ,  $\text{BaBiNaTeO}_6$  and  $\text{BaLaNaTeO}_6$   
35 [18, 19], it could be suggested that  $\text{SrLaLiTeO}_6$  has good dielectric abilities.

36 Apart from that, the properties of double perovskites materials mainly depend on B–site cations  
37 arrangements which able to modify the structural phase transition, electrical or magnetic properties.  
38 The position of B– and B'–cations in octahedral are alternating if the size difference is large meanwhile  
39 random placement of the B– and B'–cations take place whenever the size difference is small. Study  
40 regarding  $\text{Ba}_2\text{ZnWO}_6$  double perovskite in microwave frequencies points out that small dope of insulator  
41 and larger size cation ( $\text{Ca}^{2+}$ ) into B–site of perovskite could affect its microwave dielectric properties  
42 [22] by altering the tolerance factor of compound. The open problem in our study related to the ability  
43 of B–site cations doping to alter the dielectric properties of Te–based double perovskite for dielectric  
44 application such as capacitor or resonator. Studies by Vilesh et al. regarding  $\text{BaBiNaTeO}_6$  and  
45  $\text{BaBiLiTeO}_6$  [18, 19] indicated that different B–site doping can influence dielectric constant and  
46 dielectric loss. However, there is no direct study regarding this B–site full cations difference and its  
47 effects towards compounds' dielectric properties. Nonetheless, since  $\text{Na}^+$  and  $\text{Li}^+$  has almost same  
48 valence electron configuration, the main difference could be their ionic size and hence, altering cations  
49 bond stress and strain to cause different structural (octahedral) tilting or distortion before affecting other  
50 aspects such as formation energy [23]. Thus, the idea in this study is to alter the octahedral tilting or  
51 distortion in Te–based double perovskite through B–site cations doping with smaller cations to tune the  
52 structure of compounds and its dielectric property accordingly.

---

53 Meanwhile, study on B-site doping in Ba<sub>2</sub>ZnWO<sub>6</sub> has been conducted [24] and demonstrated B-site  
54 cations doping with electrically conductive characteristic has potential to yield difference on optical  
55 property of double perovskite compound. Cations with good conductivity which doped into B-site is  
56 vital in controlling charge carrier's movement or Fermi energy level inside perovskite's lattice structure,  
57 hence, reducing optical band gap ( $E_{opt}$ ). This will take effect simultaneously with the effect of structural  
58 distortion onto optical band gap since distortion can affect the band gap [21]. By doping smaller cation  
59 with electrically conductive trait into B-site of SrLaLiTeO<sub>6</sub>, the dominant effect whether reducing or  
60 widening of its  $E_{opt}$  can be seen. Hence, determining the potential applications for the studied  
61 compounds.

62 Therefore, investigating the effects of B-site cation doping in SrLaLiTeO<sub>6</sub> with Mn<sup>6+</sup> (0.255 Å) on its  
63 structural, dielectric and optical properties is an interesting endeavour and this work would deal to  
64 ascertain these effects.

65

## 66 **2. Materials and Methods**

67 Polycrystalline powders of SrLaLiTe<sub>1-x</sub>Mn<sub>x</sub>O<sub>6</sub> ( $x = 0.02, 0.04, 0.06, 0.08, 0.10$ ) were synthesized using  
68 a solid-state reaction method. High-purity ( $\geq 99.99\%$ ) of strontium carbonate (SrCO<sub>3</sub>), lithium carbonate  
69 (Li<sub>2</sub>CO<sub>3</sub>), lanthanum oxide (La<sub>2</sub>O<sub>3</sub>), manganese (III) oxide (Mn<sub>2</sub>O<sub>3</sub>) and tellurium dioxide (TeO<sub>2</sub>)  
70 powders from Sigma-Aldrich are used as raw materials. The chemical powders have been mixed at  
71 stoichiometric ratios with total mass of 3.5 g. The samples then grinded in agate mortar by pestle for 1  
72 h to achieve good homogeneity. After grinding process, the mixed powder sample then pressed into  
73 pellet at pressure of 4–5 KPa using hydraulic press. The pellet was then placed on an alumina crucible  
74 and calcinated in a box furnace at 850 °C for 10 h with heating rate of 15 °C/min and cooling rate of 1  
75 °C/min. The sintering process followed with 900 °C for 10 h with heating rate of 15 °C/min and cooling  
76 rate of 1 °C/min. This action was expected to maintain the obtained stoichiometry close to the desired  
77 oxygen stoichiometry [25]. The phase(s) of the final products were analysed by using XRD patterns  
78 collected by X-ray powder diffractometer PANanalytical model Xpert PRO MPD diffractometer  
79 equipped with a Cu K $\alpha$  source from 10° to 90°. General Structure Analysis System (GSAS) and  
80 Graphical User Interface (i.e. EXPGUI) software [26, 27] were used for Rietveld refinement [28] prior  
81 visualized in Visualisation for Electronic Structural Analysis (VESTA) program. Peak shape was  
82 modelled by pseudo-Voigt function refined together with cell parameter, scale factor, zero factor and

83 background function. For Fourier transform infra-red (FTIR) study, samples prepared by mixing  
84 thoroughly with potassium bromide (KBr) and the FTIR reflectance spectra were recorded in FTIR–  
85 Raman Drift Nicolet 6700 equipment ranging from 400 to 1500  $\text{cm}^{-1}$ . The surface morphology of the  
86 sintered pellets and constituent elements was obtained by conducting FESEM and energy dispersive X–  
87 ray (EDX) characterizations by using SU 8000, Hitachi, Japan equipment. The dielectric and modulus  
88 with frequency range of 50 Hz to 1 MHz studies were collected by using a HIOKI 3532–50 LCR Hi  
89 Tester connected to a computer while keeping the electrode pellets in sandwich geometry. Optical study  
90 performed by using Lambda 750, Perkin Elmer, Waltham, USA equipment for 2 to 5  $\text{h}\nu$  range.

91

### 92 **3. Results and discussions**

93 Figure 1 shows the refined XRD data of  $\text{SrLaLiTe}_{1-x}\text{Mn}_x\text{O}_6$  where  $x = 0.02$  (Mn 0.02),  $x = 0.04$  (Mn  
94 0.04),  $x = 0.06$  (Mn 0.06),  $x = 0.08$  (Mn 0.08), and  $x = 0.10$  (Mn 0.10) by the Rietveld refinement  
95 method. In the graph, red crosses lines are observed data, the black solid line is the calculated pattern  
96 and the blue solid line is the difference. Green ticks indicate the allowed Bragg reflections. From these  
97 plot, all compounds have formed in a single phase, with slight impurity peak present (marked with  
98 asterisk). The peak at  $44.5^\circ$  in compound Mn 0.02 and Mn 0.04 related to the residual of manganese  
99 oxide in samples. The obtained reliability ( $\chi^2$ ) was 2.178, 1.903, 1.647, 2.419 and 1.948 for  $x = 0.02$ ,  
100 0.04, 0.06, 0.08 and 0.10, respectively which show good reliability of results. Good agreement between  
101 observed and calculated interplanar spacings ( $d$ -values) indicates that all these compounds crystallize in  
102  $P2_1/n$  monoclinic structure. The refined lattice parameters of  $a$ ,  $b$  and  $c$  were in 5.57–5.63 Å, 5.58–5.61  
103 Å and 7.1–7.92 Å range, respectively for all compounds. All compounds possessed  $\alpha = 90^\circ$  and  $\gamma = 90^\circ$ ,  
104 whereas  $\beta = 90.37^\circ$ ,  $90.25^\circ$ ,  $89.93^\circ$ ,  $90.05^\circ$  and  $90.10^\circ$  for  $x = 0.02$ , 0.04, 0.06, 0.08 and 0.10,  
105 respectively. The refined unit cell volume,  $V$  for each compound was 248.7, 247.7, 248.5, 249.5 and  
106 249.9 Å<sup>3</sup>, respectively. The trend was not in agreement with the doping of smaller size of  $\text{Mn}^{6+}$  into  
107 larger  $\text{Te}^{6+}$  cations. Table 1 shows the complete parameters that were obtained from the refinement.  
108 Figure 2 shows refined structure of  $\text{SrLaLiTe}_{1-x}\text{Mn}_x\text{O}_6$  from  $bc$  plane. This figure revealed presence of  
109 doped  $\text{Mn}^{6+}$  into  $\text{Te}^{6+}$  alongside  $\text{Li}^+$  at B-site octahedral structure.  $\text{Mn}^{6+}/\text{Te}^{6+}$  and  $\text{Li}^+$  alternately  
110 positioned between each other and being surrounded by six  $\text{O}^{2-}$  atoms in each octahedron. A-site cations  
111 ( $\text{Sr}^{2+}$  and  $\text{La}^{3+}$ ) placed between octahedral to fill up spaces in the structure. In all compounds,  $\text{Li}^+$  placed  
112 at (0.5, 0, 0) and  $\text{Te}^{6+}$  at (0, 0.5, 0). Tolerance factor,  $\tau$  calculated by equation [21],

$$\tau = \frac{\frac{R_a + R_{a'}}{2} + R_o}{\sqrt{2}(\frac{R_b + R_{b'}}{2} + R_o)} \quad (1)$$

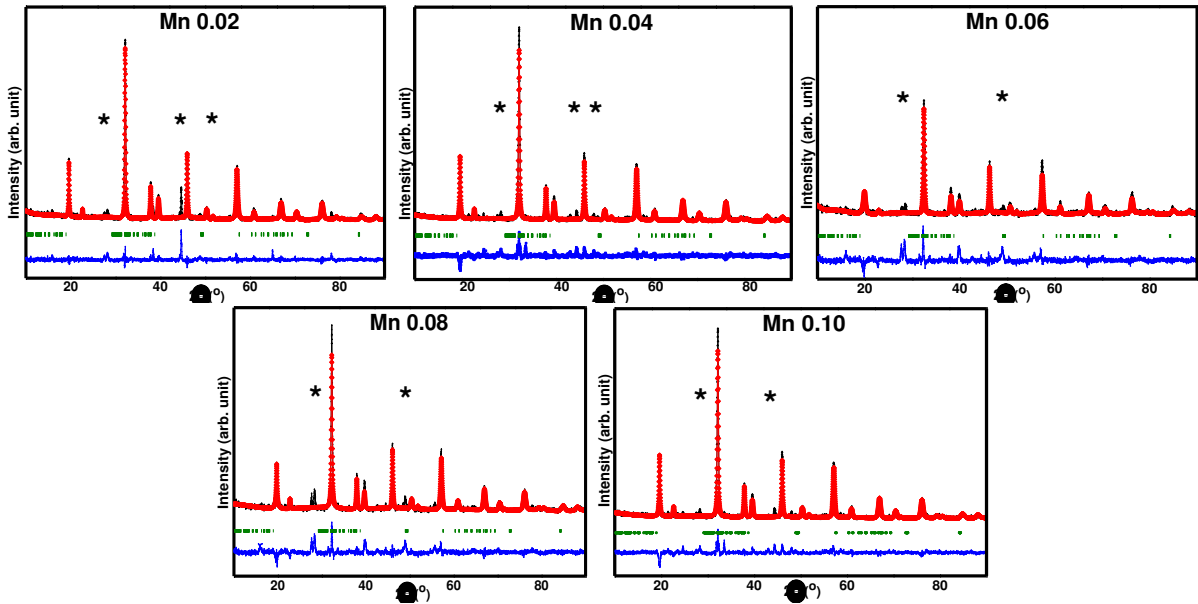
113  
 114 where  $R_a$  and  $R_{a'}$  represent radius of A-site cations ( $\text{Sr}^{2+}$  and  $\text{La}^{3+}$ ),  $R_b$  and  $R_{b'}$  represent radius of B-site  
 115 cations ( $\text{Li}^+$  and  $\text{Te}^{6+}/\text{Mn}^{6+}$ ) and  $R_o$  represents radius of oxygen anion ( $\text{O}^{2-}$ ), respectively. Size of each  
 116 ionic radius used were 1.44 Å (CN:12) for  $\text{Sr}^{2+}$ , 1.36 Å (CN:12) for  $\text{La}^{3+}$ , 0.76 Å (CN:6) for  $\text{Li}^+$ , 0.56 Å  
 117 (CN:6) for  $\text{Te}^{6+}$ , 0.255 Å (CN:6) for  $\text{Mn}^{6+}$  and 1.40 Å (CN:6) for  $\text{O}^{2-}$  [29]. The calculated  $\tau$  were  
 118 presented in Table 1 where  $\tau = 0.963$  for Mn 0.02,  $\tau = 0.964$  for Mn 0.04,  $\tau = 0.965$  for Mn 0.06,  $\tau =$   
 119  $0.967$  for Mn 0.08 and  $\tau = 0.968$  for Mn 0.10. The increment of  $\tau$  towards value of 1 (the ideal cubic  
 120 structure) showed the positive effect of doping  $\text{Mn}^{6+}$  in reducing distortion in perovskite structure. The  
 121 increment indicates that the doping of smaller ionic into B-site does aid in layered formation of A-site.  
 122 Besides, the value of octahedra tilting angle in each compound were calculated by using equation :

$$\phi = \frac{180 - \theta}{2} \quad (2)$$

123  
 124 where  $\theta$  represents average (Li–O–Te/Mn) bond angles [30]. The obtained tilting angle for all  
 125 compounds were  $9.6^\circ$ . Basically, no change of tilting angle was observed or calculated. This indicate  
 126 that tilting angle cannot be affected by small doping into pristine  $\text{SrLaLiTeO}_6$ . The average Li–O–Te  
 127 bond angle for each compound are the same and in agreement with unaffected tilting angle of octahedral  
 128 structures. Length of (B–O) and (A–O) bonds showed increasing trend as doping concentration  
 129 enhanced. The increase most probably due to the smaller ionic radius doping and for that reason, causing  
 130 each bond in A- and B-site to elongate to accommodate the unaffected tilting of octahedrons. The  
 131 crystallite size,  $D$  was calculated using the following Scherrer equation [31]:

$$D = \frac{K\lambda}{\beta(\theta) \cos \theta} \quad (3)$$

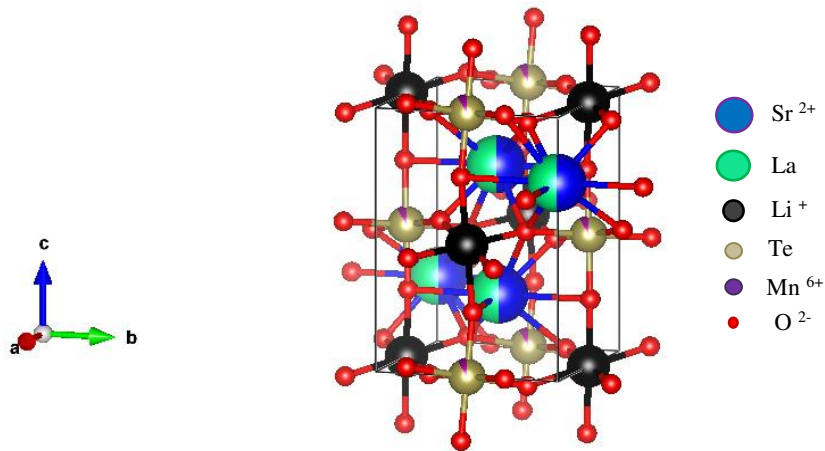
132  
 133 where  $K$  represents constant (0.94),  $\lambda$  represents the wavelength of XRD,  $\beta$  represents the full width at  
 134 half maximum and  $\theta$  represents the angle of peak of XRD. The calculated  $D$  for each compound were  
 135 28.99, 20.19, 23.48, 26.84 and 26.41 nm for Mn 0.02, Mn 0.04, Mn 0.06, Mn 0.08 and Mn 0.10,  
 136 respectively. Increasing trend of  $D$  from Mn 0.04 to Mn 0.08 indicates that  $\text{Mn}^{6+}$  dopant results in a  
 137 better crystallization as doping increased. Reduced  $D$  in Mn 0.10 may be related to formation of small  
 138 amount of impurities.



139

140

141 Figure 1: Rietveld refinement of XRD pattern of  $\text{SrLaLiTe}_{1-x}\text{Mn}_x\text{O}_6$  ( $x = 0.02, 0.04, 0.06, 0.08$  and  $0.10$ ).



142

143 Figure 2: Visual image of refined XRD of  $\text{SrLaLiTe}_{1-x}\text{Mn}_x\text{O}_6$  from  $bc$  plane.

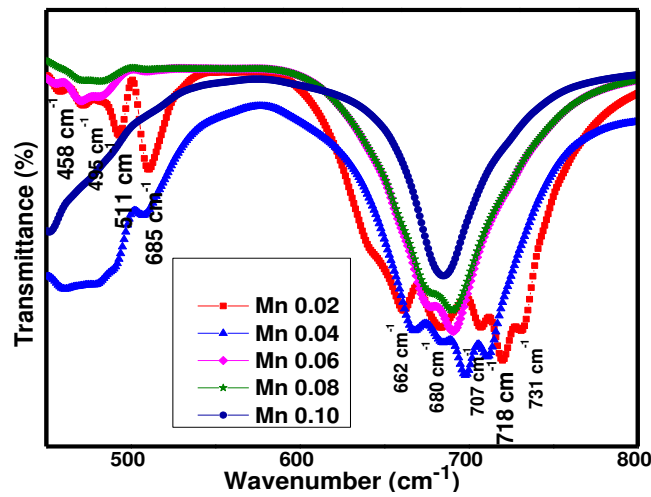
144 Table 1: Lattice parameters, unit cell volume, bond angles, bond lengths, fit goodness, tolerance factor ( $\tau$ ), and  
 145 tilting angle ( $\phi$ ) in  $\text{SrLaLiTe}_{1-x}\text{Mn}_x\text{O}_6$  ( $x = 0.02, 0.04, 0.06, 0.08, 0.10$ ) as obtained from Rietveld refinement  
 146 and crystallite size from XRD characterization.

Compounds	Mn 0.02	Mn 0.04	Mn 0.06	Mn 0.08	Mn 0.10
<b>Lattice parameter</b>					
$a$ (Å)	5.598(8)	5.578(10)	5.621(4)	5.628(2)	5.595(2)
$b$ (Å)	5.607(1)	5.614(8)	5.582(4)	5.591(8)	5.630(2)
$c$ (Å)	7.926(5)	7.911(16)	7.919(6)	7.923(3)	7.933(2)
$\alpha$	90.00°	90.00°	90.00°	90.00°	90.00°
$\beta$	90.37°	90.25°	89.93°	90.05°	90.10°
$\gamma$	90.00°	90.00°	90.00°	90.00°	90.00°
Unit cell Vol., $V$ (Å <sup>3</sup> )	248.7	247.7	248.5	249.5	249.9
<b>Bond length (Å)</b>					
Li-O <sub>1</sub> (x 2)	2.123(6)	2.119(5)	2.122(4)	2.126(5)	2.125(7)
Li-O <sub>2</sub> (x 2)	2.085(6)	2.081(5)	2.086(4)	2.089(4)	2.087(8)
Li-O <sub>3</sub> (x 2)	2.064(11)	2.060(8)	2.063(6)	2.065(6)	2.067(9)
Aver. < Li-O >	2.091(8)	2.087(6)	2.090(5)	2.093(5)	2.093(8)
Te-O <sub>1</sub> (x 2)	1.934(5)	1.933(4)	1.935(4)	1.937(4)	1.940(7)

<b>Te-O<sub>2</sub> (x 2)</b>	1.936(5)	1.935(4)	1.934(3)	1.937(3)	1.941(7)
<b>Te-O<sub>3</sub> (x 2)</b>	1.924(10)	1.920(8)	1.921(6)	1.924(5)	1.925(8)
<b>Aver. &lt; Te-O &gt;</b>	1.931(7)	1.929(5)	1.930(4)	1.933(4)	1.935(7)
<b>Mn-O<sub>1</sub> (x 2)</b>	1.934(5)	1.933(4)	1.935(4)	1.937(4)	1.940(7)
<b>Mn-O<sub>2</sub> (x 2)</b>	1.936(5)	1.935(4)	1.934(3)	1.937(3)	1.941(7)
<b>Mn-O<sub>3</sub> (x 2)</b>	1.924(10)	1.920(8)	1.921(6)	1.924(5)	1.925(8)
<b>Aver. &lt; Mn-O &gt;</b>	1.931(7)	1.929(5)	1.930(4)	1.933(4)	1.935(7)
<b>Aver. &lt; Sr-Sr &gt;</b>	3.962(19)	3.958(18)	3.962(8)	3.965(11)	3.969(24)
<b>Aver. &lt; La-La &gt;</b>	3.962(19)	3.958(18)	3.962(8)	3.965(11)	3.969(24)
<b>Bond angles (°)</b>					
<b>Li-O<sub>1</sub>-Te/Mn</b>	155.0(12)	155.0(10)	155.1(9)	155.1(9)	155.1(12)
<b>Li-O<sub>2</sub>-Te/Mn</b>	160.2(4)	160.2(4)	160.3(6)	160.3(8)	160.3(5)
<b>Li-O<sub>3</sub>-Te/Mn</b>	167.1(8)	167.1(6)	167.1(4)	167.1(4)	167.1(7)
<b>Aver. &lt; Li-O-Te/Mn &gt;</b>	160.7(8)	160.7(7)	160.8(6)	160.8(7)	160.8(8)
<b>Fit Goodness</b>					
$\chi^2$	2.178	1.903	1.647	2.419	1.948
<b>R<sub>p</sub> (%)</b>	0.117	0.133	0.138	0.135	0.119
<b>R<sub>wp</sub> (%)</b>	0.167	0.171	0.179	0.183	0.158
<b>Tolerance factor and tilting angle</b>					
<b>Tol. factor, <math>\tau</math></b>	0.963	0.964	0.965	0.967	0.968
<b>Tilting angle, <math>\phi</math></b>	9.6	9.6	9.6	9.6	9.6
<b>Crystallite Size (nm)</b>					
<b>Crystallite Size, <i>D</i></b>	28.99	20.19	23.48	26.84	26.41

147

148 Figure 3 illustrates the FTIR spectrum of SrLaLiTe<sub>1-x</sub>Mn<sub>x</sub>O<sub>6</sub> ( $x = 0.02, 0.04, 0.06, 0.08, 0.10$ ) compounds. As a  
149 comparison, Mn 0.02 present significant peaks between 400 to 1000 cm<sup>-1</sup>. Peaks at 458 and 472 cm<sup>-1</sup> in Mn  
150 0.02 can be assigned to Li-O bond stretching vibrations [32]. The emergence of medium peaks at 495 cm<sup>-1</sup> can  
151 be assigned to antisymmetric stretching vibrations ( $\nu_1$ ) in Te(Li)O<sub>6</sub> octahedra. At the same time, strong peaks at  
152 662, 680, 710, and 731 cm<sup>-1</sup> can be assigned to the symmetric stretching vibration ( $\nu_2$ ) of the Te(Li)O<sub>6</sub> octahedra  
153 [19, 33-36]. It is clear that as dopant concentration increased, there were more quenched of peaks. This is  
154 understandable since the Te-O-Li should be reduced when the doping Mn<sup>6+</sup> into Te<sup>6+</sup> took place to form Mn/Te-  
155 O-Li bonds. Nonetheless, peak at 720 cm<sup>-1</sup> in Mn 0.02 can be suggested due to introduction of Mn<sup>6+</sup> with none  
156 of peak present at the same wavenumber for pristine SrLaLiTeO<sub>6</sub> [37]. Besides, this peak started to shift to lower  
157 wavenumbers indicating the increment of abundance of Mn-O bonds as dopant increased with Mn 0.10 depicts  
158 the Mn-O bonds vibration peak at 685 cm<sup>-1</sup>. Meanwhile, most of the existing peaks redshifted as dopant content  
159 increases implying the increase of bond length. These results are in accordance with the Rietveld refinement and  
160 tolerance factor. Summary of the peaks obtained were tabulated in Table 2.

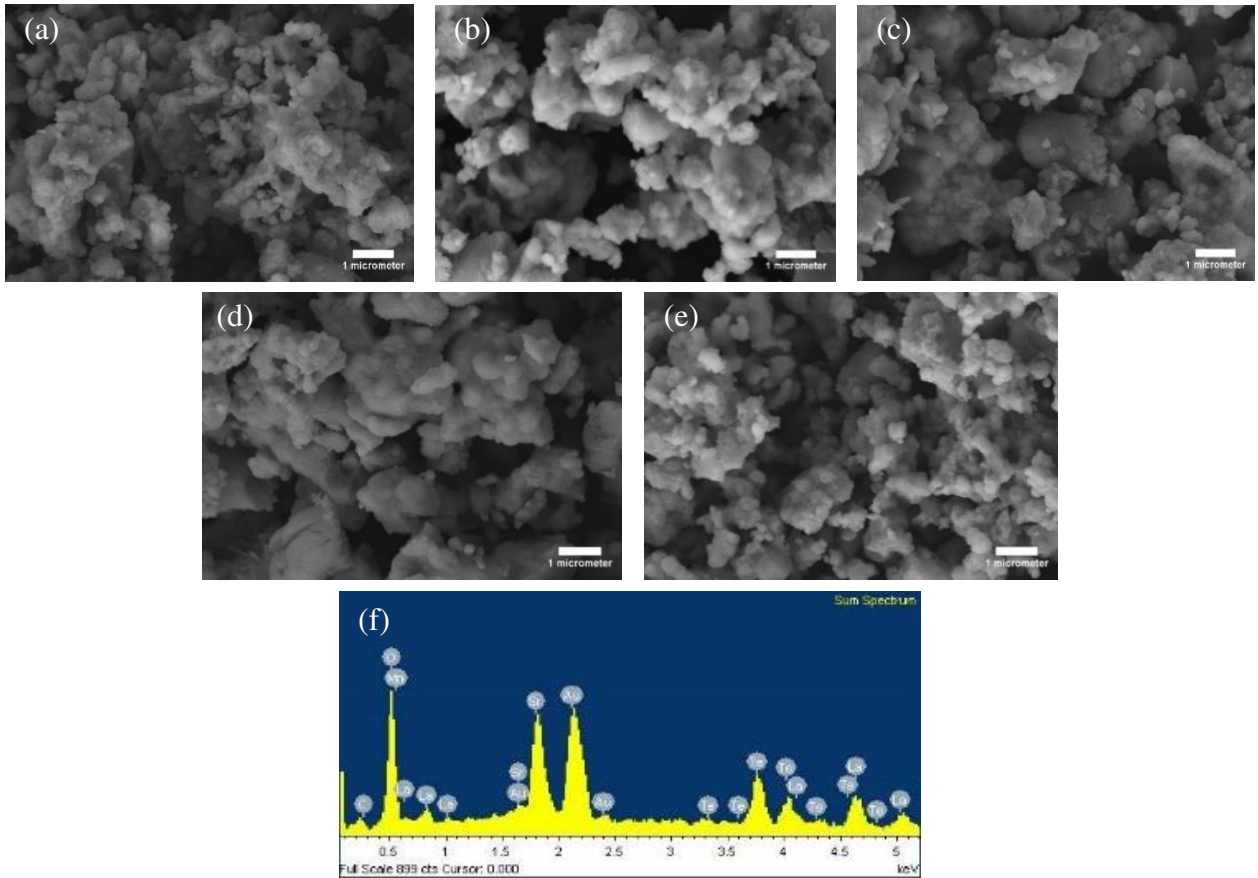


161  
162 Figure 3: FTIR spectrum of  $\text{SrLaLiTe}_{1-x}\text{Mn}_x\text{O}_6$  ( $x = 0.02, 0.04, 0.06, 0.08, 0.10$ ).

163 Table 2: Samples' peaks and their designations from FTIR characterization.

Compounds' wavenumber peaks ( $\text{cm}^{-1}$ )					Designation
Mn 0.02	Mn 0.04	Mn 0.06	Mn 0.08	Mn 0.10	
458	460	457	-	-	Stretching Li–O
474	480	457	470	453	
493	491	482	483	481	$\nu_1$
511	507	509	507	515	$\nu_1$
662	-	-	-	-	$\nu_2$
680	-	-	-	-	$\nu_2$
707	684	678	678	-	$\nu_2$
731	711	-	-	-	$\nu_2$
718	698	691	690	685	Stretching of Mn–O

164  
165 Figure 4 exhibits the morphology of  $\text{SrLaLiTe}_{1-x}\text{Mn}_x\text{O}_6$  ( $x = 0.02, 0.04, 0.06, 0.08, 0.10$ ) compounds. The  
166 formation of agglomerated particles with same shape and size distribution of most grains were clear. Grains size  
167 were increased from 1.03–1.97  $\mu\text{m}$ , 1.10–1.17  $\mu\text{m}$ , 1.97–2.07  $\mu\text{m}$ , 2.14–2.26  $\mu\text{m}$  and 1.21–1.43  $\mu\text{m}$  as dopant  
168 concentration increased from  $x = 0.02$  to  $x = 0.10$ . This variation trend is same with trend of crystallite size  
169 variation. The increasing trend in size of grain in Mn 0.04 to Mn 0.08 most probably related to decrease in  
170 structural distortion when smaller ionic radius ( $\text{Mn}^{6+}$ ) content increased [23] and thus, affecting rate of  
171 nucleation [38]. Other possible reason may be due to the reduction of grain boundaries energy as small cationic  
172 size Mn content increased and lead to grain size enhancement. EDX graph in Figure 4(f) representing constituted  
173 elements in Mn 0.08. This graph confirms that this compounds contains elements of the prepared raw material  
174 composition, except Au which originate from coating in sample preparation for FESEM characterization. Other  
175 compounds show almost same trend of EDX graph as in Figure 4(f).



176

177

178

179 Figure 4: FESEM images (10 K magnification) of  $\text{SrLaLiTe}_{1-x}\text{Mn}_x\text{O}_6$  ((a)  $x=0.02$ , (b)  $x=0.04$ , (c)  $x=0.06$ , (d)  
 180  $x=0.08$  and (e)  $x=0.10$ ), and (f) EDX plot of  $x=0.08$ .

181 The UV–vis diffuse reflectance measurements for  $\text{SrLaLiTe}_{1-x}\text{Mn}_x\text{O}_6$  ( $x = 0.02, 0.04, 0.06, 0.08, 0.10$ ) were  
 182 performed at ambient temperature and in the wavelength range of 200–800 nm. Figure 5(a) displays the UV–  
 183 vis spectra as a function of wavelength,  $\lambda$ . Compared to pristine  $\text{SrLaLiTeO}_6$  [39], there are strong absorption  
 184 bands observed at whole 300–600 nm range. It was probably because of the charge transfer between localised  
 185  $1d$  orbital of  $\text{Mn}^{6+}$  and localised  $2p$  orbital of  $\text{O}^{2-}$ . As  $\text{Mn}^{6+}$  dopant increases, the reduction of reflectance value  
 186 of compound indicates the increase of the absorbance ability. When  $\text{Mn}^{6+}$  doped into  $\text{Te}^{6+}$  site, Mn band can be  
 187 created inside the gap. At low concentration of dopant, the band gap width is not hugely affected. With increasing  
 188  $\text{Mn}^{6+}$  dopant, the widths of these Mn bands increase and bands could overlap together. This implies the changes  
 189 in the reflectance spectra. The broadening of the reflectance spectra as dopant added indicate the probability of  
 190 Mn band widening and overlapping of the bands with increasing  $\text{Mn}^{6+}$  dopant [40].

191 Figure 5(b) exhibits the UV–vis diffuse spectra of  $\text{SrLaLiTe}_{1-x}\text{Mn}_x\text{O}_6$  plotted from Kubelka-Munk equation [21],

192

$$\mathbf{F(R)} = \frac{(1-R)^2}{2R} \quad (4)$$

193 where  $R$  represents diffuse reflectance. By taking the intercept of the extrapolations to zero absorption with the  
194 photon energy axis, value of absorption edge can be obtained. The values of band gap energy can be calculated  
195 by applying equation:

$$196 \quad E_g = \frac{1240}{\lambda} \quad (5)$$

197 where  $\lambda$  represents wavelength of absorption edge. Meanwhile, Figure 5(c) show the spectra plotted from Tauc's  
198 equation:

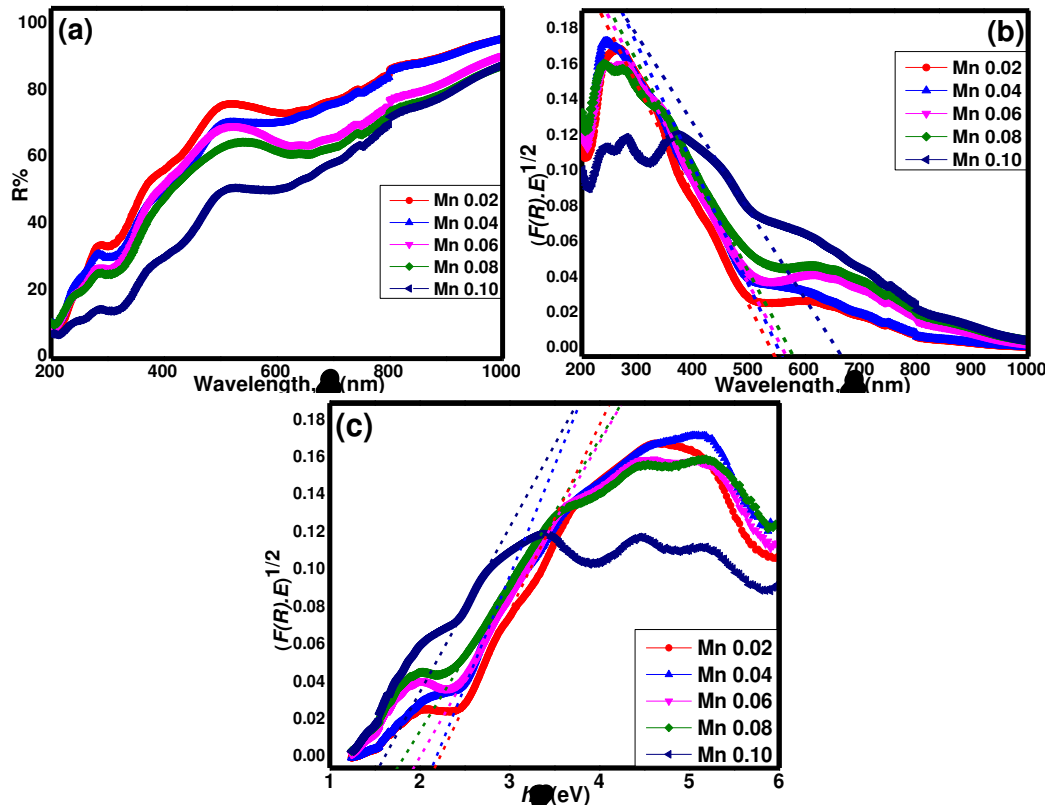
$$199 \quad [F(R)hv]^n = A(hv - E_{opt}) \quad (6)$$

200 where  $hv$  represents energy,  $A$  represents proportional constant and  $E_{opt}$  represents gap energy. The value of  $n$   
201 depends on the characteristics of transition in a material i.e.  $n = 1/2$  (direct allowed transition),  $n = 2$  (indirect  
202 allowed transition),  $n = 3/2$  (direct forbidden transition) and  $n = 3$  (indirect forbidden transition) [21].

203 Figure 5(b) shows the absorbance cut-off wavelength increases with increasing  $Mn^{6+}$  content. Meanwhile,  
204 Figure 5(c) shows fitting of  $n = 1/2$  looked the most fitted to the graph and hence, implies that the optical band  
205 gap in this compound has allowed and direct shift of electrons from valence band to conduction band where only  
206 absorption of photon took place. The comparable values of  $E_{opt}$  obtained from both Kubelka–Munk and Tauc  
207 plots are tabulated in Table 3. All obtained  $E_{opt}$  values are in range of 2.18 eV till 1.55 eV, indicating the  
208 semiconductor optical properties. The value getting smaller from Mn 0.02 until Mn 0.10, indicating the best  
209 optical semiconducting ability in Mn 0.10. These values show much reduction of  $E_{opt}$  compared to pristine  
210 SrLaLiTeO<sub>6</sub> [21]. Literature [40–42] has reported that the  $E_{opt}$  is associated with the presence of impurity energy  
211 levels within the band gap of the materials. As wider Mn energy bands (impurity bands) formed with higher  
212 dopant concentration, this change will reduce the distance between bands and consequently reduce the  $E_{opt}$ . On  
213 the other hand, reduction in structural distortion when  $Mn^{6+}$  doped into pristine compound is the other reason to  
214 reduce  $E_{opt}$ . Opposite explanation regarding effect of distortion onto band gap has been discussed in other report  
215 [21]. Besides, oxygen vacancies are the other possible factor which are able to promote the formation of impurity  
216 energy levels within the band gap [42] in all compounds. It is accepted that oxygen vacancies can contribute to  
217 the results in this work. However, the monoclinic structure as well as lattice parameters of all compounds are  
218 comparable to the stoichiometric in SrLaLiTeO<sub>6</sub> on previous report [21]. Hence, it is suggested that differences  
219 in oxygen content among the compounds are small and should not have major influence on the measured  
220 properties. There is other report that reveal the same trend of  $E_{opt}$  of other compound of doping with  $Mn^{2+}$   
221 realized [43]. The absorbance spectra in Fig. 5(b) shows that all compounds' optical band gaps are in visible

222 light range, makes SrLaLiTe<sub>1-x</sub>Mn<sub>x</sub>O<sub>6</sub> possible for photovoltaic applications with further study to increase the  
 223 electronic conductivity.

224



225

226

227 Figure 5: (a) The diffuse reflection spectra, (b) Kubelka–Munk plot and (c) Tauc plot of SrLaLiTe<sub>1-x</sub>Mn<sub>x</sub>O<sub>6</sub> ( $x =$   
 228 0.02, 0.04, 0.06, 0.08, 0.10) (dotted line are the fitting for optical band gap).

229 Table 3: Absorbed wavelength from Kubelka–Munk plot, optical band gap calculated from Kubelka–Munk plot  
 230 and optical band gap obtained from Tauc plot in SrLaLiTe<sub>1-x</sub>Mn<sub>x</sub>O<sub>6</sub> ( $x = 0.02, 0.04, 0.06, 0.08, 0.10$ ).

Compounds	Mn 0.02	Mn 0.04	Mn 0.06	Mn 0.08	Mn 0.10
$\lambda_{abs}$ (nm)	544	556	565	578	664
$E_{opt abs}$ (eV)	2.27	2.23	2.19	2.15	1.87
$E_{opt Tauc}$ (eV)	2.18	2.14	1.95	1.77	1.55

231

232 Figure 6(a) shows the variation of  $\epsilon'$  vs frequency between 50 Hz to 1 MHz for SrLaLiTe<sub>1-x</sub>Mn<sub>x</sub>O<sub>6</sub> ( $x = 0.02,$   
 233 0.04, 0.06, 0.08, 0.10) compounds at room temperature. The variation of  $\epsilon'$  with frequency showed almost the  
 234 same trend for each compound, with respect to frequencies below or above 100 Hz. For frequencies below 100  
 235 Hz, the compounds show almost similar variation of  $\epsilon'$  with frequency which  $\epsilon'$  dropped abruptly with  
 236 frequency from a higher initial value. At frequencies above 100 Hz, the decrease of  $\epsilon'$  was moderately and slow  
 237 to reach the minimum value at 1 MHz. However, started from 400 kHz, there is a decrement of gradient of  $\epsilon'$   
 238 only in Mn 0.08 before continuing to gradual drop to be the highest value of  $\epsilon'$  between all compounds at 1

239 MHz. Figure 6(a) (inset) showed changes of  $\epsilon'$  at specific frequencies of 250 kHz, 500 kHz and 750 kHz and  
240 average size of grains for all compounds. It is clear that aside of  $\epsilon'$  in Mn 0.02, the increasing trend of  $\epsilon'$  is clear  
241 with the peak value shown by Mn 0.08 before decreased significantly at higher doping. This  $\epsilon'$  peak obviously  
242 interrelated with peak of grain size of Mn 0.08.

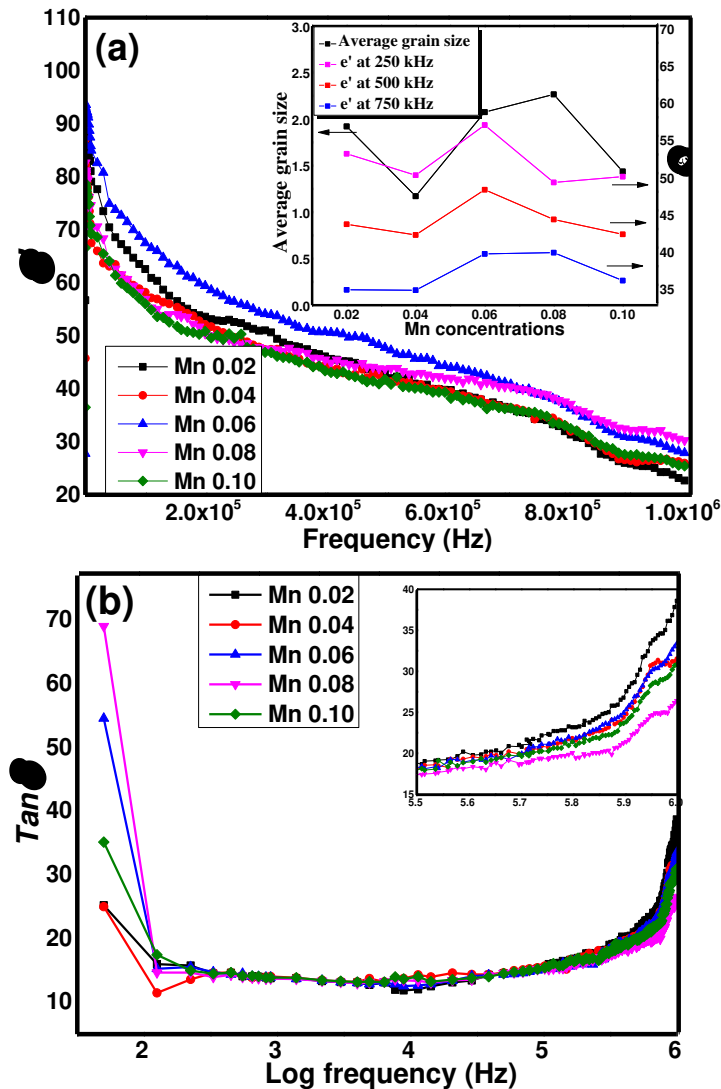
243 Figure 6(b) shows the dielectric loss,  $Tan \delta$  variation in  $SrLaLiTe_{1-x}Mn_xO_6$  ( $x = 0.02, 0.04, 0.06, 0.08, 0.10$ ) at  
244 room temperature. This figure showed drop of  $Tan \delta$  at frequencies of less than 500 Hz before relatively flat  
245 pattern at frequencies above 500 Hz. Compounds with different dopant concentrations exhibit almost the same  
246 increasing pattern from 10 kHz to 1 MHz. Figure 6(b) (inset) shows the  $Tan \delta$  at 300 kHz and above. This  
247 increase indicates the possibility of relaxation peak existence at frequencies higher than 1 MHz.

248 The real component of dielectric constant,  $\epsilon'$  illustrates the aligning ability of electrical dipoles in compounds  
249 with the external electric field. The initial decrease of  $\epsilon'$  at frequencies less than 100 Hz for all compounds in  
250 Figure 6(a) was suggested to be due to the heavy dipoles which mainly consists of space charge dipoles  
251 originated from defects in grain boundaries. These heavy dipoles are the ones that unable to follow the electric  
252 field alternation when frequencies were increased. Presence of oxygen vacancies in insulating compounds can  
253 reduce the phonon modes in structure, hence, causing space charge polarization [44].  $\epsilon'$  drop in low frequencies  
254 was in alignment with high losses in  $Tan \delta$  at the same frequencies as in Figure 6(b).

255  $Tan \delta$  represents the energy loss in the compounds in the midst of electric field alternation. DC conduction loss  
256 might be another factor in assisting the drop of the  $\epsilon'$ . Nevertheless, the gradient in plot of  $\ln \epsilon'$  against  $\ln \omega$   
257 (not shown) did not show magnitude close to (-1) to prove the presence of this factor. Apparently, there are no  
258 clear difference in frequencies below than 100 Hz range after doping in each compound. However, at  
259 frequencies higher than 100 Hz, medium and light sized dipoles did contribute in  $\epsilon'$  response. They are mainly  
260 comprised of orientational, ionic and electronic dipoles.  $\epsilon'$  values keep on decreasing as frequencies increased.  
261 Nonetheless, the slowly decrease of  $\epsilon'$  response in Mn 0.08 compared to other  $\epsilon'$  compounds can be pertained to  
262 the probability of higher abundance of medium sized of electrical dipoles compared to light ones. This variation  
263 is related to smallest  $Tan \delta$  in the compound at frequencies above 400 kHz. Compared to pristine  $SrLaLiTeO_6$   
264 [39], there is enhancement of  $\epsilon'$  value in all  $Mn^{6+}$  doped  $SrLaLiTeO_6$ .

265 The variation of  $\epsilon'$  response can be explained in terms of its interrelation with average grain size in inset of  
266 Figure 6(a). Larger grains size can form larger medium sized dipoles and probability of higher amount of  
267 medium sized dipoles. As a consequence, production of larger electrical dipole moments can take place in

268 contrast to smaller grains. Accordingly, higher polarization effect can take place. This then suit to explain the  
 269 relationship between variation in  $\epsilon'$  and average grain size. Mn 0.08 was clearly possessed higher  $\epsilon'$  at higher  
 270 frequencies might be due to this factor. Other reports that are related to this interrelation between  $\epsilon'$  and grain  
 271 size has been recorded before [45].



272

273

274 Figure 6: (a)  $\epsilon'$  and (b)  $\tan \delta$  of  $\text{SrLaLiTe}_{1-x}\text{Mn}_x\text{O}_6$  ( $x = 0.02, 0.04, 0.06, 0.08, 0.10$ ), (inset of (a)) average grain  
 275 sizes and  $\epsilon'$  at respective frequencies for each compound, (inset of (b))  $\tan \delta$  at 300 kHz and higher frequencies.

276

277

#### 4. Conclusion

278

279

280

281

282

$\text{SrLaLiTe}_{1-x}\text{Mn}_x\text{O}_6$  ( $x = 0.02, 0.04, 0.06, 0.08, 0.10$ ) double perovskites have been successfully prepared  
 by using solid state reaction method and all compounds formed in monoclinic,  $P2_1/n$  symmetry. The  
 presence of peaks at certain wavenumbers confirms the formation of  $\text{Te}^{6+}/\text{Mn}^{6+}-\text{O}-\text{Li}^+$  octahedral  
 structure. The grain size of the compounds gets larger towards higher concentration doping. The  
 reduction of optical band gap can be deduced because of the doping of  $\text{Mn}^{6+}$  cations to reduce the

283 distance between highest HOMO and lowest LUMO in the compound. Nevertheless, all compounds  
284 showed absorption within visible light range which make the application for compounds in  
285 optoelectronic device such as solar cell can be realized with modifications on its electrical conductivity or  
286 tuning its  $E_{opt}$ . Highest dielectric constant and lowest dielectric losses recorded by Mn 0.08. This  
287 behaviour can be elucidated on the basis of grain size. Further study related to annealing temperature or  
288 other means can be done to increase the dielectric constant in the future.

289

## 290 **Declarations**

291 **Availability of data and materials** Not applicable

292 **Competing Interests** We have no competing interests.

293 **Funding** This work was financially supported by the Ministry of Education Malaysia (MOE) and  
294 Universiti Teknologi MARA (UiTM), grant number 600-IRMI/FRGS5/3 (356/2019).

295 **Authors' Contributions** M. Z. M. Halizan carried out the lab work, heavily participated in data analysis,  
296 drafted the manuscript; Dr. Z. Mohamed participated in data analysis and revised the manuscript, and Prof. A.  
297 K. Yahya critically revised the manuscript. All authors gave final approval for publication and agree to be held  
298 accountable for the work performed therein.

299 **Ethical Approval** Our investigation was carried out in full accordance with the ethical guidelines of our  
300 research institution and in compliance with Malaysian legislation.

301 **Acknowledgements** Authors would like to thank all lecturers and lab members of Superconductor  
302 Physics Lab, UiTM Shah Alam for fruitful discussions regarding our research works.

303

304

## 305 **References**

1. W. Xu, F. Li, Z. Cai, Y. Wang, F. Luo, and X. Chen, *Journal of Materials Chemistry C* **4**(41),96515 (2016).
2. T. R. Shrout, S. J. Zhang, R. Eitel, and C. Stringer, C. A. Randall, In 14th IEEE International Symposium on Applications of Ferroelectrics, ISAF-04, IEEE, 126-129 (2004).
3. H. Farahani, R. Wagiran, and M. N. Hamidon, *Sensors* **14**(5), 7881-939 (2014).
4. S. Fujii, Y. Shimada, K., Utsumi, and Y. Saito, U.S. Patent No. 4,574,255, 1986, Washington, DC: U.S. Patent and Trademark Office.

- 
5. R. I. Scott, M. Thomas, and C. Hampson, *Journal of the European Ceramic Society* **23**(14), 2467-7 (2003).
  6. W. Wersing, *Current Opinion in Solid State and Materials Science* **1**(5), 715-31 (1996).
  7. I. M. Reaney and D. Iddles, *Journal of the American Ceramic Society* **89**(7), 2063-72 (2006).
  8. J. Burschka, N. Pellet, S. J. Moon, R. Humphry-Baker, P. Gao, M. K. Nazeeruddin, and M. Grätzel, *Nature* **499**(7458), 316-9 (2013).
  9. A. Mei, X. Li, L. Liu, Z. Ku, T. Liu, Y. Rong, M. Xu, M. Hu, J. Chen, Y. Yang, and M. Grätzel *Science* **345**(6194), 295-8 (2014).
  10. J. H. Im, C. R. Lee, J. W. Lee, S. W. Park, and N. G. Park, *Nanoscale* **3**(10), 4088-93 (2011).
  11. W. J. Yin, T. Shi, and Y. Yan, *Applied Physics Letters* **104**(6), 063903 (2014).
  12. A. J. Hauser, J. M. Lucy, G. W. Gaultois, M. R. Ball, J. R. Soliz, Y. Choi, O. D. Restrepo, W. Windl, J. W. Freeland, D. Haskel, and P. M. Woodward. *Physical Review B* **89**(18), 180402 (2014).
  13. H. M. Yang, W. Y. Lee, H. Han, B. W. Lee, C. S. Kim, *Journal of applied physics* **93**(10), 6987-9 (2003).
  14. J. Sánchez-Benítez, J. A. Alonso, M. J. Martínez-Lope, A. de Andres, and M. T. Fernández-Díaz, *Inorganic chemistry* **49**(12), 5679-85 (2010).
  15. S. Suzuki, A. Honda, N. Iwaji, S. I. Higai, A. Ando, H. Takagi, H. Kasatani, and K. Deguchi, *Physical Review B* **86**(6), 060102 (2012).
  16. A. Dias, G. Subodh, M. T. Sebastian, and R. I. Moreira, *Journal of Raman Spectroscopy* **41**(6), 702-706 (2010).
  17. A. Dias, G. Subodh, M. T. Sebastian, M. M. Lage, and R. L. Moreira, *Chemistry of Materials* **20**(13), 4347-4355 (2008).
  18. V. L. Vilesh and G. Subodh, *Ceramics International* **43**(15), 12718-23 (2007).
  19. V. L. Vilesh and G. Subodh, *Ceramics International* **44**(11), 12036-12041 (2018).
  20. G. King and P. M. Woodward, *Journal of Material Chemistry* **20**(28), 5785-5796 (2010).
  21. B. Amrithakrishnan and G. Subodh, *Materials Research Bulletin* **93**,177-82 (2017).
  22. A. Gandhi and S. Keshri, *Ceramics International* **41**(3), 3693-3700 (2015).
  23. T. Ishigaki, Z. S. Nikolic, T. Watanabe, N. Matsushita, and M. Yoshimura, *Solid State Ionics* **180**(6-8), 475-9 (2009).
  24. Y. A. Alsabah, M. S. AlSalhi, A. A. Elbadawi, and E. M. Mustafa, *Journal of Alloys and Compounds*

- 701**, 797-805 (2007).
25. Z. Harrell, E. Enriquez, A. Chen, P. Dowden, B. Mace, X. Lü, Q. Jia, and C. Chen, *Applied Physics Letters* **110**(9), 093102 (2007).
  26. W. Yansen, D. Kim, K. J. Parwanta, C. Liu, and B. W. Lee, *Current Applied Physics* **15**(2),120-123 (2015).
  27. K. R. Kumar, N. H. Kumar, G. Markandeyulu, J. A. Chelvane, V. Neu, and P. D. Babu, *Journal of magnetism and magnetic materials* **320**(21), 2737-40 (2008).
  28. H. Rietveld, *Journal of applied Crystallography* **2**(2),65-71 (1969).
  29. R. D. Shannon, *Acta crystallographica section A: crystal physics, diffraction, theoretical and general crystallography* **32**(5), 751-67 (1976).
  30. J. W. Bos and A. P. Attfield, *Physical Review B* **70**(17), 174434 (2004).
  31. C. A. Triana, D. L. Téllez, J. A. Rodríguez, F. Fajardo, and J. Roa-Rojas, *Materials Letters* **82**, 116-9 (2012).
  32. V. Rathod, A. V. Anupama, R. V., Kumar, R. V., V. M. Jali, and B. Sahoo, *B. Vibrational Spectroscopy* **92**, 267-272 (2017).
  33. S. C. Lal, A. Rajan, and G. Subodh, *Materials Today: Proceedings*, **4**(2), 4396-4402 (2017).
  34. K. Li, H. Lian, R. Van Deun, and M. G. Brik, *Dyes and Pigments* **162**, 214-21 (20149).
  35. A. E. Lavat, R. C. Mercader, and E. J. Baran, *Journal of alloys and compounds* **508**(1), 24-7 (2010).
  36. F. Ding, M. L. Nisbet, H. Yu, W. Zhang, L. Chai, P. S. Halasyamani, and K. R. Poeppelmeier, *Inorganic chemistry* **57**(13),7950-6 (2008).
  37. M. Z. M. Halizan, et al., *Digest Journal of Nanomaterials and Biostructures* **15**(3), 733-741 (2020).
  38. B. Prajapati, S. Kumar, M. Kumar, S. Chatterjee, A.K. Ghosh, A.K. Ghosh, *J. Mater. Chem. C* **5** (2017) 4257.
  39. M. Z. M. Halizan, Z. Mohamed, and A. K. Yahya, *Materials Research Express* **7**(8), 086301 (2020).
  40. Dang, N. V., Dung, N. T., Phong, P. T., & Lee, I. J. *Physica B: Condensed Matter* **457**, 103-107 (2015).
  41. N. Bajpai, M. Saleem, and A. Mishra, *Journal of Materials Science: Materials in Electronics*, 1-13 (2020).
  42. A. Priya, E. Sinha, and S. K. Rout, *Solid state sciences* **20**, 40-45 (2013).
  43. S. S. Abdullahi, S. Güner, Y. K. I. M. Musa, B. I. Adamu, and M. I. Abdulhamid, *NAMP J* **35**, 241-

---

246 (2016).

44. M. Youssef, K. J. Van Vliet, and B. Yildiz, *Physical review letters* **119**(12), 126002 (2017).
45. P. Nayak, T. Badapanda, A. K. Singh, and S. Panigrahi, *RSC Advances* **7**(27), 16319-16331 (2017).

# Figures

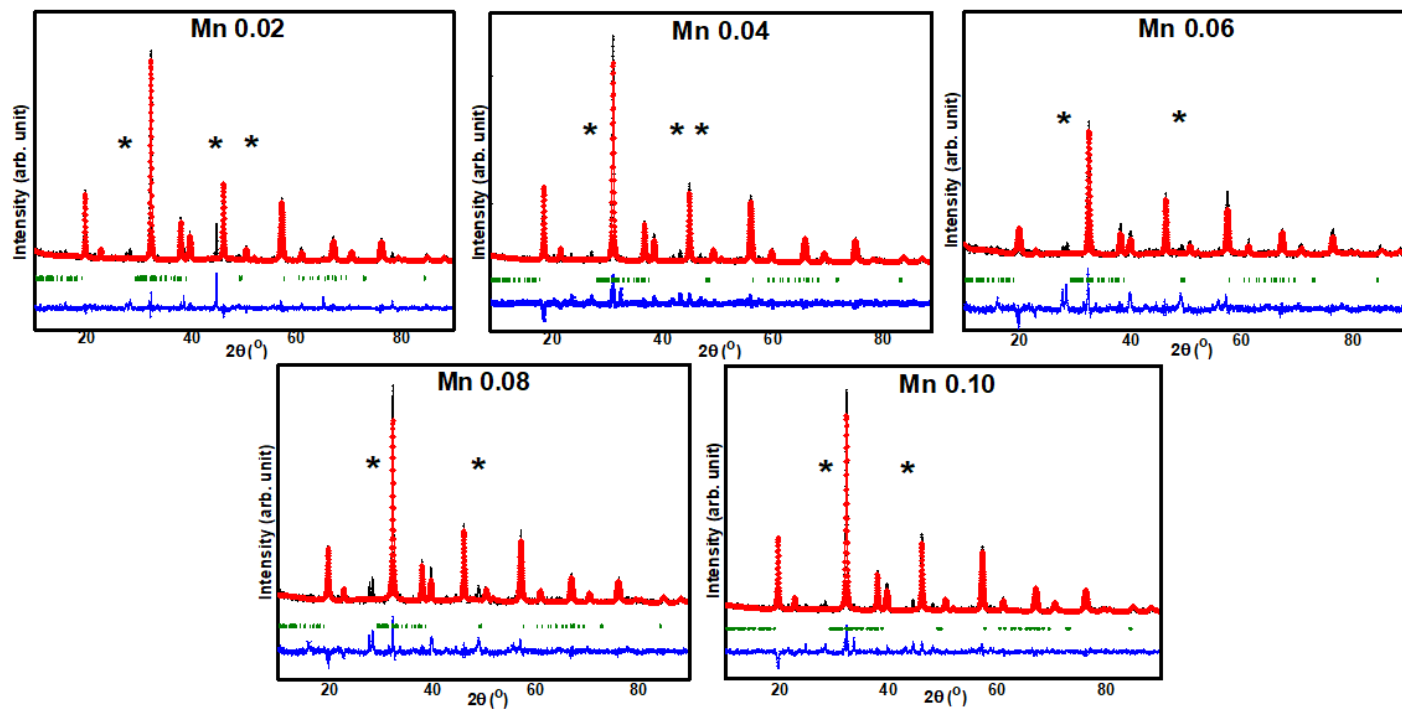


Figure 1

Rietveld refinement of XRD pattern of SrLaLiTe<sub>1-x</sub>Mn<sub>x</sub>O<sub>6</sub> (x = 0.02, 0.04, 0.06, 0.08 and 0.10).

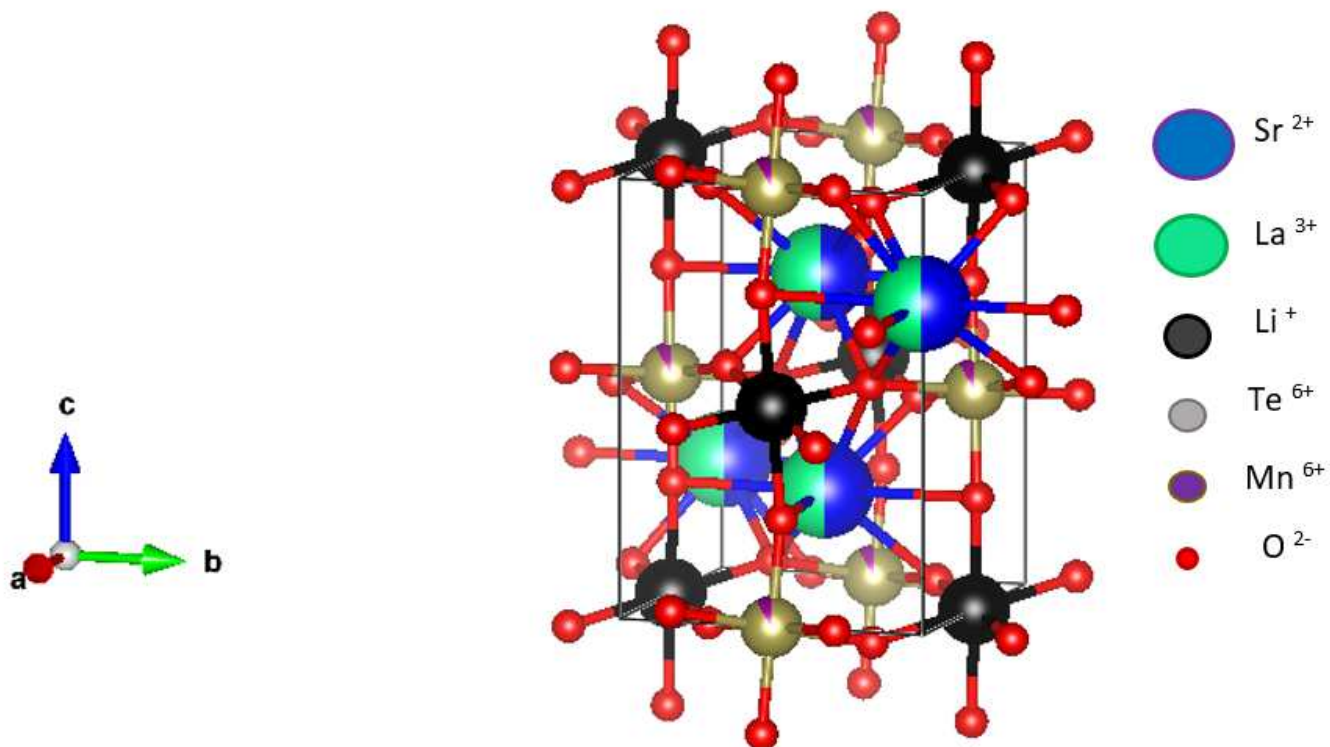


Figure 2

Visual image of refined XRD of SrLaLiTe<sub>1-x</sub>MnxO<sub>6</sub> from bc plane.

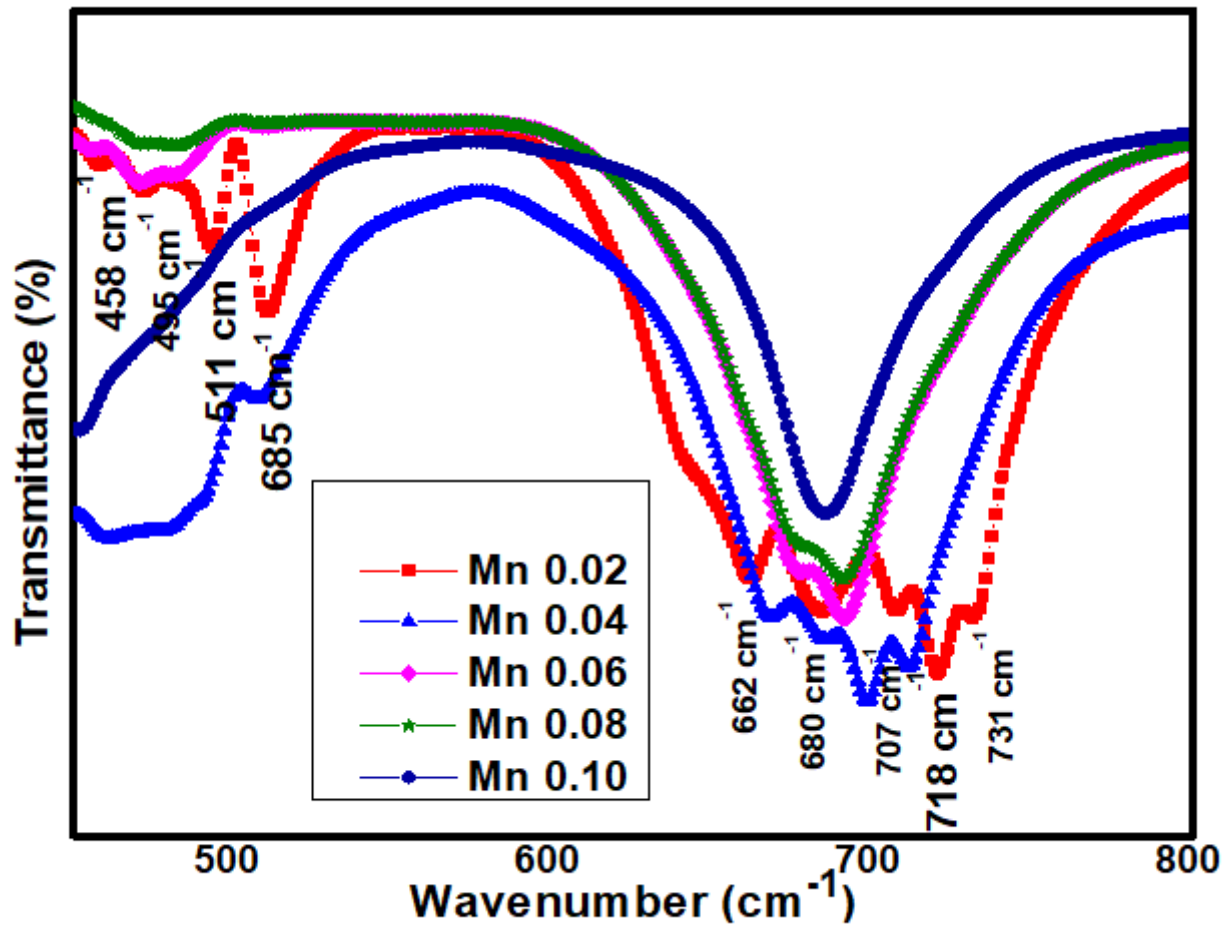
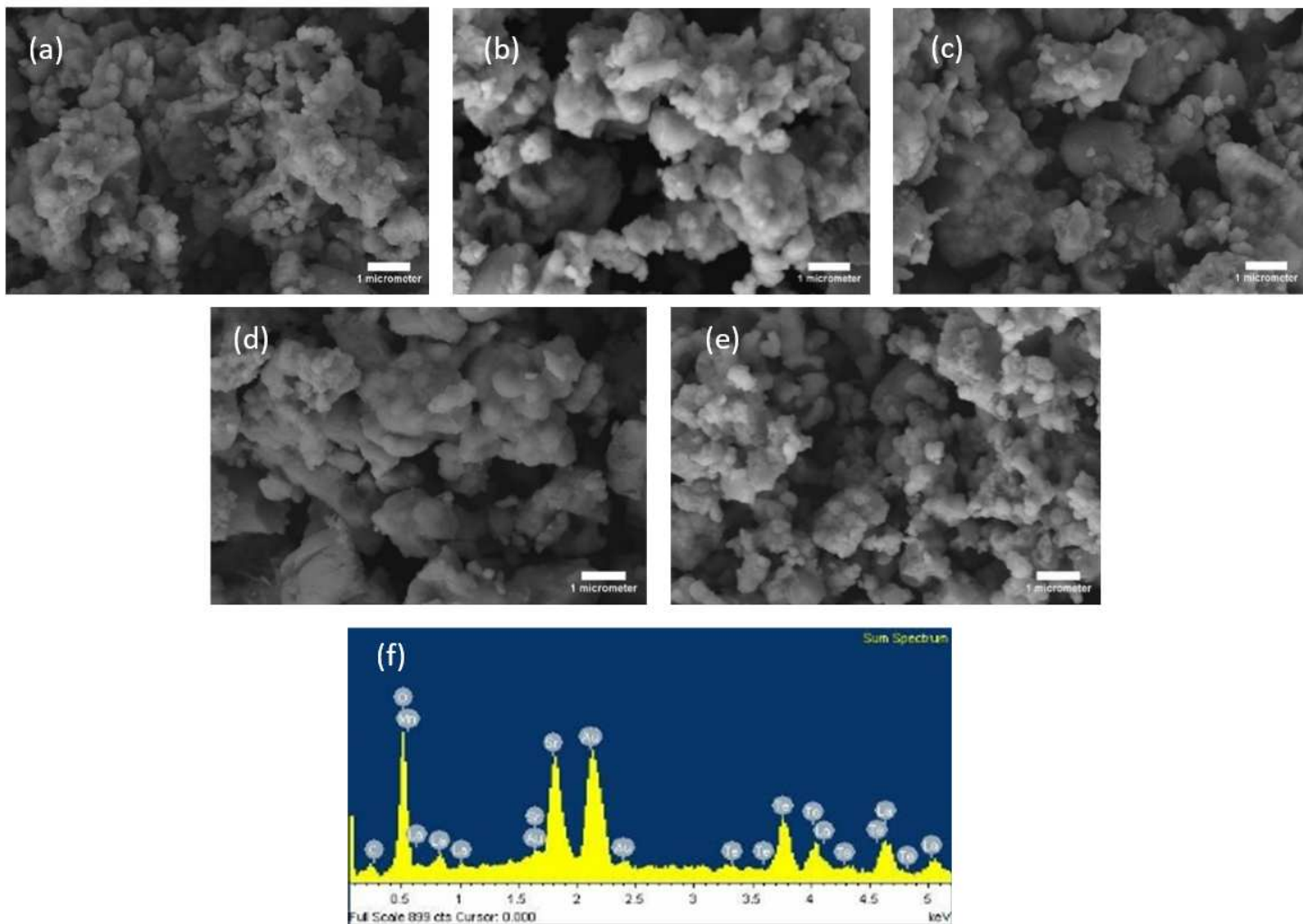


Figure 3

FTIR spectrum of SrLaLiTe<sub>1-x</sub>MnxO<sub>6</sub> (x = 0.02, 0.04, 0.06, 0.08, 0.10).



**Figure 4**

FESEM images (10 K magnification) of  $\text{SrLaLiTe}_{1-x}\text{Mn}_x\text{O}_6$  ((a)  $x=0.02$ , (b)  $x=0.04$ , (c)  $x=0.06$ , (d)  $x=0.08$  and (e)  $x=0.10$ ), and (f) EDX plot of  $x=0.08$ .

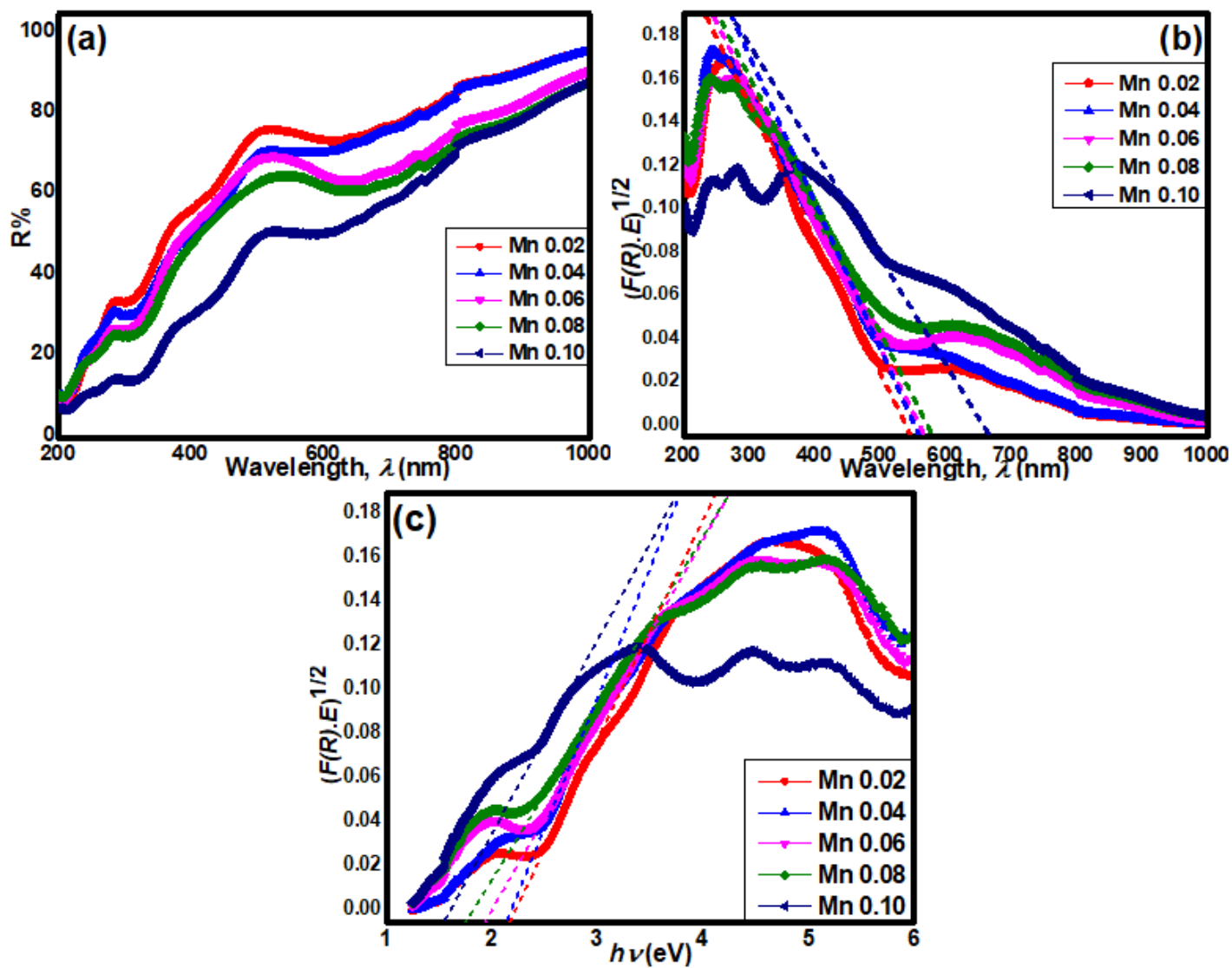


Figure 5

(a) The diffuse reflection spectra, (b) Kubelka–Munk plot and (c) Tauc plot of SrLaLiTe<sub>1-x</sub>Mn<sub>x</sub>O<sub>6</sub> (x = 0.02, 0.04, 0.06, 0.08, 0.10) (dotted line are the fitting for optical band gap).

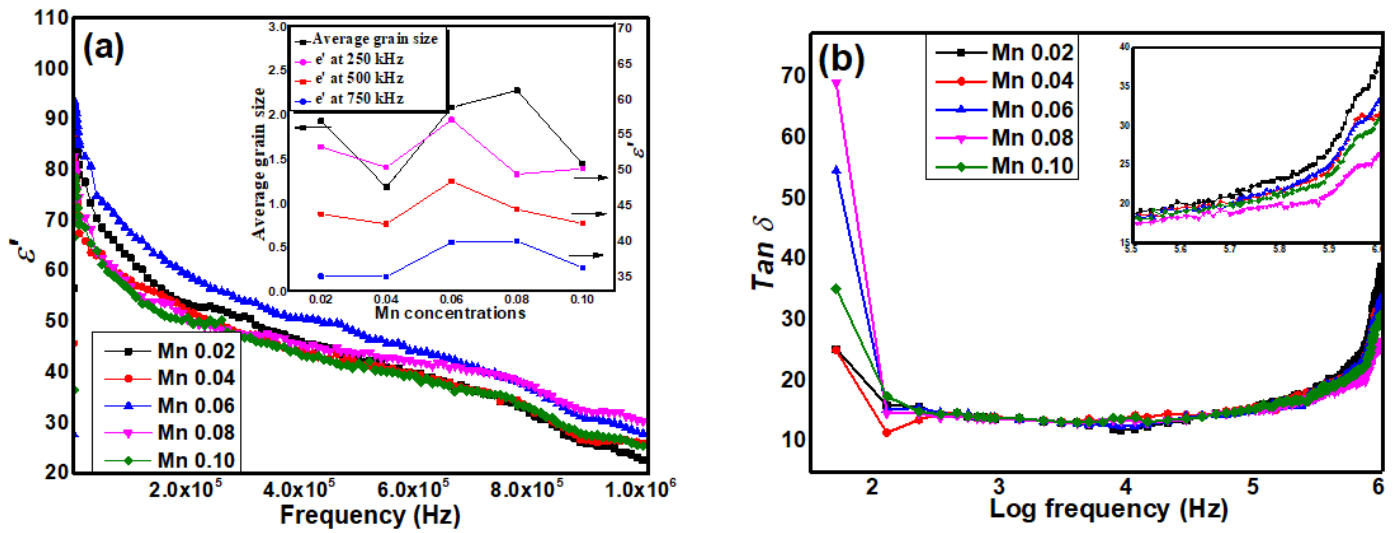


Figure 6

(a)  $\epsilon'$  and (b)  $\tan \delta$  of SrLaLiTe<sub>1-x</sub>Mn<sub>x</sub>O<sub>6</sub> (x = 0.02, 0.04, 0.06, 0.08, 0.10), (inset of (a)) average grain sizes and  $\epsilon'$  at respective frequencies for each compound, (inset of (b))  $\tan \delta$  at 300 kHz and higher frequencies.